JOURNAL OF SPACECRAFT AND ROCKETS
Vol. 30, No. 6, November–December 1993

Thermo-Chemical Nonequilibrium Effects on the Aerothermodynamics of Aerobraking Vehicles

Basil Hassan,* Graham V. Candler,† and David R. Olynick*
North Carolina State University, Raleigh, North Carolina 27695

A three-dimensional computational fluid dynamics algorithm is developed to study the effect of chemical and thermal nonequilibrium on blunt body aerodynamics. Both perfect gas and five species air reacting gas models are used to compute the flow over the Apollo command module. The reacting gas air mixture is assumed to be governed by a translational-rotational temperature and a vibrational temperature. The Navier-Stokes computations are compared to wind-tunnel and flight-aerodynamic data from the Apollo missions. The effects of chemical reaction and vibrational excitation on lift-to-drag ratio and trim angle are investigated. It is shown that including real gas effects results in a lower trim angle and L/D than predicted by nonreacting gas wind-tunnel simulations. The reacting gas numerical results are consistent with flight data from the unmanned Apollo AS-202 mission, whereas the perfect gas computations agree with the extrapolated preflight wind-tunnel results.

Nomenclature

A, B, C	= flux Jacobian matrices
c_{vs}	= species translational-rotational specific heat at constant volume, J/kg · K
$\mathfrak{D}$	= diagonal matrix
E	= total energy per unit volume, J/m^3
E_v	= vibrational energy per unit volume, J/m^3
e_{vs}	= species specific vibrational energy, J/kg
F, G, H	= Cartesian flux vectors
I	= identity matrix
h_s	= species specific enthalpy, J/kg
h_s^0	= species heat of formation, J/kg
k_b	= backward reaction rate, m^3/kmol · s or m^6/kmol^2 · s
k_f	= forward reaction rate, m^3/kmol · s
M	= Mach number, or reaction partner
M_s	= species molecular weight, kg/kmol
nd	= number of diatomic species
ne	= number of elements
ns	= number of species
Pr	= Prandtl number
p	= pressure, N/m^2
q	= translational-rotational heat flux, W/cm^2
q_v	= vibrational heat flux, W/cm^2
R	= universal gas constant, 8314.3 J/kmol · K
T	= translational-rotational temperature, K
T_v	= vibrational temperature, K
U	= vector of conserved quantities
u, v, w	= Cartesian velocities, m/s
$\tilde{u}_s$	= species diffusion velocity, m/s
V	= grid cell volume, m^3
W	= source vector
w_s	= chemical source term, kg/m^3 · s
w_v	= vibrational source term, J/m^3 · s
x, y, z	= Cartesian coordinates, m
Z	= source Jacobian matrix
α	= angle of attack, deg
γ	= ratio of specific heats
θ_{vs}	= species characteristic temperature of vibration, K
Λ	= diagonal matrix containing eigenvalues
μ	= coefficient of viscosity, kg/m · s
ξ, η, ζ	= computational coordinates
ρ	= total density, kg/m^3
$\tilde{\rho}_e$	= elemental density, kg/m^3
ρ_s	= species density, kg/m^3
τ	= shear stress, N/m^2
τ_s	= chemical relaxation time, s
τ_v	= vibrational relaxation time, s

Subscripts

e	= elemental value
I	= inviscid terms
i, j, k	= position in computational space
s	= species value
stag	= stagnation value
V	= viscous term
x, y, z	= derivative
$+$	= positive moving wave
$-$	= negative moving wave
∞	= freestream value

Superscripts

n	= iteration level
T	= transpose
$'$	= variables in computational space

Introduction

THE renewed interest in the area of hypersonic aerodynamics has brought forth the need for efficient computational fluid dynamics (CFD) algorithms to aid in the design process. The concept of aerobraking for use in future missions to Mars has shown promise for Mars entry and Earth return trajectories.[1,2] The use of CFD has become important in predicting hypersonic flows due to its relative cost efficiency when compared to the cost of flight experiments and wind-tunnel testing, as well as the lack of adequate ground facilities to produce the correct aerothermodynamic environment. CFD has become feasible mainly due to recent advances in the supercomputing industry and in algorithm development. However, to make full use of the benefits to be gained from CFD, improvements in physical models must be made to correctly simulate the aerodynamics and heating experienced during an aerobrake maneuver.

Walberg[3] has shown that a significant amount of flight and ground test data exists and can be used to bolster confidence in computational techniques. For high energy ($V_\infty > 10$ km/s) Earth return missions, the primary set of flight data is from

Received July 28, 1992; revision received Nov. 30, 1992; accepted for publication Dec. 7, 1992.

*Research Assistant, Mars Mission Research Center. Student Member AIAA.

†Assistant Professor, Mars Mission Research Center. Member AIAA.

the Apollo missions of the late 1960s. These data are useful since they cover a wide range of the aerothermodynamic environment of interest. Hillje[4,5] compiled aerodynamic force coefficient and trim angle data on two unmanned Apollo missions, AS-202 and AS-501, and Lee and Goodrich[6] presented pressure distributions and convective and radiative heat transfer on the Apollo 4 and 6 missions. Hillje[4] showed that the flight trim angle of attack was lower than predicted at the initial flight entry condition near a Mach number of 28. This resulted in a total lift-to-drag ratio that was approximately 18% lower than predicted in wind-tunnel tests. This type of behavior is seen all the way down to a Mach number of 6, although the difference decreases with decreasing Mach number. Walberg[3] states that a reason for this difference may be due to the chemical dissociation and nonequilibrium effects.

Air is made up mostly of O_2 and N_2. Around flight Mach numbers of 8–10, the diatomic species begin to dissociate. In addition to the chemical effects, significant molecular vibrational excitation occurs which is closely coupled to the chemical dissociation. Ionization also becomes important at vehicle Mach numbers above about 20. For the low density and high velocity flows to be considered, nonequilibrium effects will be very important. The type of thermo-chemical model used will affect the shape of the bow shock in front of the vehicle due to chemical reactions in the flowfield. The shock shape directly affects the surface pressure distribution and thus the vehicle's pitching moment and trim angle. This effect has not been studied computationally on aerobrakes except in two dimensions where only qualitative agreement with flight experiment was obtained.[7] The purpose of this investigation is to use computational methods to further examine the trim angle issue and determine to what degree the chemistry and vibrational excitation affect the re-entry aerodynamics of blunted aerobraking vehicles.

To carry out this study, a computationally efficient numerical scheme is desired to solve the Navier-Stokes equations. Implicit time advancement schemes[8–17] are attractive for finding steady-state solutions of chemically reacting flows. In general, the characteristic time scales for dissociation and vibration are many orders of magnitude lower than that of the convective fluid flow. As a result, explicit time steps must be of the order of the chemical time scales to maintain stability. Implicit techniques, however, can maintain stability with larger time steps. Although implicit techniques require more CPU time per iteration, they generally result in fewer iterations and a lower overall CPU time than that produced by explicit algorithms.

One of the major concerns in computing three-dimensional thermo-chemical nonequilibrium flows is the increased amount of CPU time and memory associated with problems of interest. Many of the implicit schemes cited involve the inversion and storage of Jacobian matrices that are of size $ns + 5$ for a multispecies gas with two temperatures. These two issues limit the size of numerical meshes even on today's supercomputers. The diagonal implicit technique of Yoon and Jameson[17] has shown great promise in overall efficiency. Candler and Olynick[18] have shown in two dimensions that with some improvements to the scheme of Eberhardt and Imlay[13] and Imlay et al.,[14] the diagonal implicit scheme is comparable to the Gauss-Seidel line-relaxation technique[10–12] in regard to overall CPU time but with significant reductions in storage. Therefore, the modified diagonal implicit method will be used in this study.

Governing Equations

A three-dimensional thermo-chemical nonequilibrium flow can be represented as

$$\frac{\partial U}{\partial t} + \frac{\partial F}{\partial x} + \frac{\partial G}{\partial y} + \frac{\partial H}{\partial z} = W \tag{1}$$

For a perfect gas, U is just

$$U = (\rho, \rho u, \rho v, \rho w, E)^T \tag{2}$$

where u, v, and w are the velocities in the x, y, and z directions, respectively. The perfect gas flux vectors will not be repeated here but can be found in the texts by Anderson et al.[19] or Hirsch.[20] Finally, the source vector W is zero for a perfect gas.

Next consider a multispecies reacting gas for air with two temperatures. The conventional choice for U and that used in Refs. 13 and 14 is

$$U = (\rho_1, \rho_2, \ldots, \rho_{ns}, \rho u, \rho v, \rho w, E_v, E)^T \tag{3}$$

However, a choice of U consistent with the modified diagonal implicit formulation of Candler and Olynick[18] is

$$U = (\tilde{\rho}_1, \ldots, \tilde{\rho}_{ne}, \rho_{ne+1}, \ldots, \rho_{ns}, \rho u, \rho v, \rho w, E_v, E)^T \tag{4}$$

where $\tilde{\rho}_e$ is the elemental density of element e. The rationale for this formulation will be made evident in the next section. The vibrational energy may be related to the vibrational temperature using a simple harmonic oscillator model

$$E_v = \sum_{s=nd} \rho_s e_{vs} = \sum_{s=nd} \rho_s \frac{R}{M_s} \frac{\theta_{vs}}{e^{\theta_{vs}/T_v} - 1} \tag{5}$$

The total energy is given by

$$E = \sum_s \rho_s (c_{vs} T + h_s^0) + E_v + \tfrac{1}{2}\rho(u^2 + v^2 + w^2) \tag{6}$$

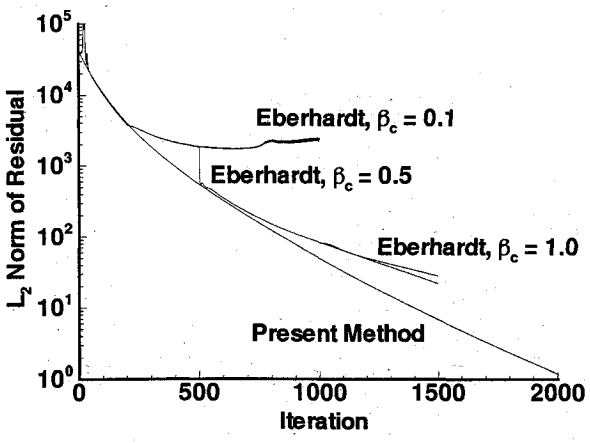

Fig. 1 Comparison of convergence rates for the proposed and original diagonal implicit methods for inviscid flow over a cylinder.

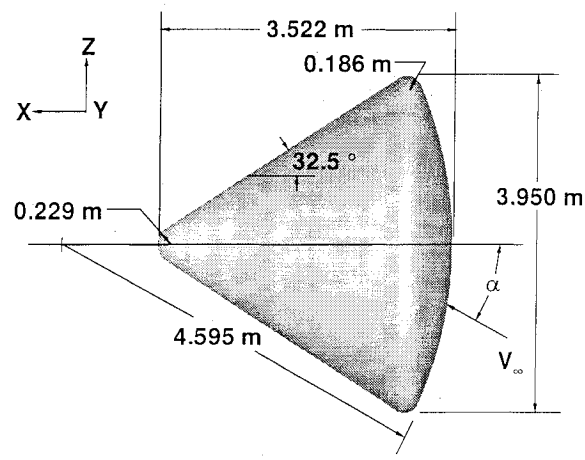

Fig. 2 Schematic of the Apollo command module geometry.

The equation of state is given by Dalton's law where

$$p = RT\sum_s \frac{\rho_s}{M_s} \tag{7}$$

For this model, the flux vector in the x direction F is

$$F = \begin{bmatrix} \tilde{\rho}_1 u \\ \vdots \\ \tilde{\rho}_{ne} u \\ \rho_{ne+1} u_{ne+1} \\ \vdots \\ \rho_{ns} u_{ns} \\ \rho u^2 + p + \tau_{xx} \\ \rho uv + \tau_{xy} \\ \rho uw + \tau_{xz} \\ \Sigma_s \rho_s e_{vs} u_s + q_{vx} \\ (E + p + \tau_{xx})u + \tau_{xy} v + \tau_{xz} w \\ \ldots + q_x + q_{vx} + \Sigma_s \rho_s h_s \tilde{u}_s \end{bmatrix} \tag{8}$$

where p is the pressure, $\tilde{u}_s$ the species diffusion velocity, and $u_s = u + \tilde{u}_s$. The species specific enthalpy is given by h_s, and q_x and q_{vx} are the translational-rotational and vibrational heat fluxes in the x direction, respectively. The flux vectors in the y and z directions have similar forms. The formulation of the viscous and heat fluxes is discussed in length by Candler.[10]

Now consider a simple reacting air model with five chemical species: N_2, O_2, NO, N, and O. For this five-species air model, there are five basic reactions that are required. These are dissociation reactions for the diatomic species and two exchange reactions involving NO.

$$\begin{aligned} N_2 + M &\rightleftharpoons N + N + M \\ O_2 + M &\rightleftharpoons O + O + M \\ NO + M &\rightleftharpoons N + O + M \\ N_2 + O &\rightleftharpoons NO + N \\ NO + O &\rightleftharpoons O_2 + N \end{aligned} \tag{9}$$

where M is a reaction partner and can be any of the above five species. Solving for the elemental densities and the densities of the reaction products, the vector of conserved quantities becomes

$$U = (\tilde{\rho}_N, \tilde{\rho}_O, \rho_{NO}, \rho_N, \rho_O, \rho u, \rho v, \rho w, E_v, E)^T \tag{10}$$

where $\tilde{\rho}_N$ and $\tilde{\rho}_O$ are the elemental densities given by

$$\frac{\tilde{\rho}_N}{M_N} = 2\frac{\rho_{N_2}}{M_{N_2}} + \frac{\rho_{NO}}{M_{NO}} + \frac{\rho_N}{M_N} \tag{11}$$

and

$$\frac{\tilde{\rho}_O}{M_O} = 2\frac{\rho_{O_2}}{M_{O_2}} + \frac{\rho_{NO}}{M_{NO}} + \frac{\rho_O}{M_O} \tag{12}$$

Note that the sum of the elemental densities is the total density. Also, because chemical reactions preserve elements, the source terms for the elemental densities are zero. Thus the new source vector W is given by

$$W = (0, 0, w_{NO}, w_N, w_O, 0, 0, 0, w_v, 0)^T \tag{13}$$

For example, the chemical source term for NO, w_{NO}, is

$$\begin{aligned} \frac{1}{M_{NO}} w_{NO} = &-\sum_s k_{f3_s} \frac{\rho_{NO}}{M_{NO}} \frac{\rho_s}{M_s} + \sum_s k_{b3_s} \frac{\rho_N}{M_N} \frac{\rho_O}{M_O} \frac{\rho_s}{M_s} \\ &+ k_{f4} \frac{\rho_{N_2}}{M_{N_2}} \frac{\rho_O}{M_O} - k_{b4} \frac{\rho_{NO}}{M_{NO}} \frac{\rho_N}{M_N} - k_{f5} \frac{\rho_{NO}}{M_{NO}} \frac{\rho_O}{M_O} \\ &+ k_{b5} \frac{\rho_{O_2}}{M_{O_2}} \frac{\rho_N}{M_N} \end{aligned} \tag{14}$$

The source terms for the other species are evaluated in a similar manner. The forward reaction rates for the dissociation reactions are based on Park's TT_v model[21] where

$$k_{fs} = k_{fs}(\bar{T}), \qquad \bar{T} = \sqrt{TT_v}$$

All other rates are functions of the translation-rotational temperature only. The chemical reaction rates are obtained from the literature.[21]

The vibrational energy equation also has a source term. This is based on the Landau-Teller model for harmonic oscillators.[22] This can be written as

$$w_v = \sum_{s=nd} \left\{ \rho_s \frac{e_{vs}^*(T) - e_{vs}}{\langle \tau_s \rangle} + w_s e_{vs} \right\} \tag{15}$$

where $\langle \tau_s \rangle$ is the average vibrational relaxation time of species s. This is obtained by number weighting the individual vibrational relaxation times from the interaction of s with itself and the other chemical species. These relaxation times are obtained from the semi-empirical expression from Millikan and White.[23] The terms e_{vs} and $e_{vs}^*(T)$ are the vibrational energy per mass contained in a simple harmonic oscillator at the local vibrational and translational temperatures, respectively. The second term in Eq. (15) results from conservation of vibrational energy during chemical reactions.[10]

Solution Procedure

In this section the diagonal implicit procedure of Yoon and Jameson and the extensions of Eberhardt et al. are discussed. A modification to this method to improve its performance for reacting gas flows is then proposed. The technique discussed here uses a modified form of Steger-Warming flux-vector splitting[24] for the spatial differencing. Break the flux F into two parts, the inviscid flux F_I and the viscous flux F_V and likewise for G and H. The flux-vector splitting method relies on the fact that the inviscid flux vectors F_I, G_I, and H_I are homogeneous in the conserved quantities U. This applies for the gas model discussed earlier and for many more general thermodynamic models. In this case,

$$F_I = \frac{\partial F_I}{\partial U} U = AU \tag{16}$$

Split the inviscid flux vector into two parts F_+ and F_- using the diagonalization

$$\begin{aligned} F_+ &= A_+ U = S^{-1} \Lambda_{A+} SU \\ F_- &= A_- U = S^{-1} \Lambda_{A-} SU \end{aligned} \tag{17}$$

where the positive elements of Λ_A, the diagonal matrix of eigenvalues, have been placed in Λ_{A+} and the negative elements in Λ_{A-}.

Employing a general coordinate transformation, the governing equation can be more easily solved in computational space such that

$$(x, y, z) \mapsto (\xi, \eta, \zeta) \tag{18}$$

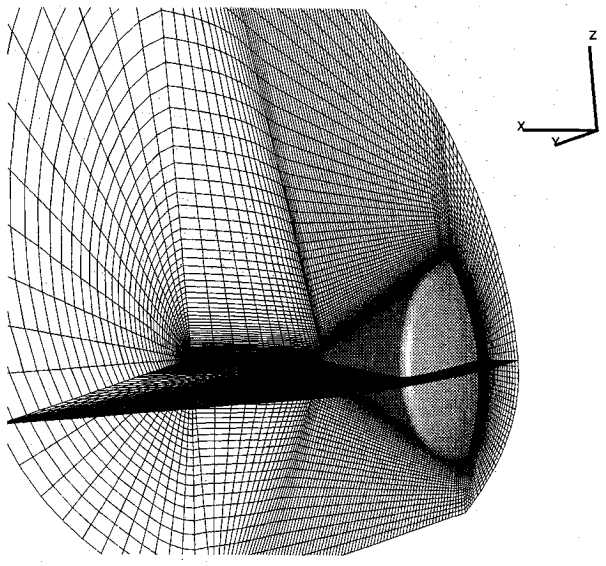

Fig. 3 Perfect gas computational grid: 110 × 26 × 70.

The transformation is given by

$$\frac{\partial}{\partial x} = \xi_x \frac{\partial}{\partial \xi} + \eta_x \frac{\partial}{\partial \eta} + \zeta_x \frac{\partial}{\partial \zeta}$$

$$\frac{\partial}{\partial y} = \xi_y \frac{\partial}{\partial \xi} + \eta_y \frac{\partial}{\partial \eta} + \zeta_y \frac{\partial}{\partial \zeta} \tag{19}$$

$$\frac{\partial}{\partial z} = \xi_z \frac{\partial}{\partial \xi} + \eta_z \frac{\partial}{\partial \eta} + \zeta_z \frac{\partial}{\partial \zeta}$$

Computational fluxes can now be defined by

$$F' = \xi_x F + \xi_y G + \xi_z H$$

$$G' = \eta_x F + \eta_y G + \eta_z H \tag{20}$$

$$H' = \zeta_x F + \zeta_y G + \zeta_z H$$

and the governing equation in computational space becomes

$$\frac{\partial U}{\partial t} + \frac{\partial F'}{\partial \xi} + \frac{\partial G'}{\partial \eta} + \frac{\partial H'}{\partial \zeta} = W \tag{21}$$

Now finite difference Eq. (21) using first-order-implicit Euler time integration in finite volume form.

$$\frac{V_{i,j,k}}{\Delta t}(U^{n+1}_{i,j,k} - U^n_{i,j,k}) + \frac{D_-}{\Delta \xi} F'^{n+1}_{+i+\frac{1}{2},j,k} + \frac{D_+}{\Delta \xi} F'^{n+1}_{-i-\frac{1}{2},j,k}$$
$$+ \frac{D_-}{\Delta \eta} G'^{n+1}_{+i,j+\frac{1}{2},k} + \frac{D_+}{\Delta \eta} G'^{n+1}_{-i,j-\frac{1}{2},k} + \frac{D_-}{\Delta \zeta} H'^{n+1}_{+i,j,k+\frac{1}{2}}$$
$$+ \frac{D_+}{\Delta \zeta} H'^{n+1}_{-i,j,k-\frac{1}{2}} = W^{n+1}_{i,j,k} \tag{22}$$

where the operators D_+ and D_- indicate forward and backward differences, respectively, and $V_{i,j,k}$ is the grid cell volume. Linearize the fluxes and the source vector in time using the appropriate Jacobians

$$F'^{n+1}_{+i+\frac{1}{2},j,k} \simeq A'^{n}_{+i+\frac{1}{2},j,k} U^n_{i,j,k} + A'^{n}_{+i+\frac{1}{2},j,k} \delta U^n_{i,j,k}$$

$$F'^{n+1}_{-i+\frac{1}{2},j,k} \simeq A'^{n}_{-i+\frac{1}{2},j,k} U^n_{i+1,j,k} + A'^{n}_{-i+\frac{1}{2},j,k} \delta U^n_{i+1,j,k}$$

$$W^{n+1}_{i,j,k} \simeq W^n_{i,j,k} + Z^n_{i,j,k} \delta U^n_{i,j,k}$$

where $\delta U^n = U^{n+1} - U^n$ and Z is the Jacobian of the source vector W with respect to U. The location where δU is evaluated depends on the direction of the flux; positive fluxes use information from the left and negative fluxes from the right. This still leaves the location of the evaluation of the flux Jacobians ambiguous because data is only stored at the cell centers. Choosing to evaluate the flux Jacobians at the same location as U, then Steger-Warming flux vector splitting[24] is obtained. This differencing scheme has been shown to be extremely dissipative in boundary layers and thus is undesirable for viscous flows.[25] However, with a simple modification, very good boundary-layer characteristics can be obtained.[25,26] This is done by evaluating the flux Jacobians as

$$A'_{+i+\frac{1}{2},j,k} = A'_+[\tfrac{1}{2}(U_{i+1,j,k} + U_{i,j,k})]$$
$$A'_{-i+\frac{1}{2},j,k} = A'_-[\tfrac{1}{2}(U_{i+1,j,k} + U_{i,j,k})] \tag{23}$$

that is, evaluate the Jacobians of both the positive and negative fluxes at the same location.

Having performed the linearization, the difference equation becomes with $\Delta\xi = \Delta\eta = \Delta\zeta = 1$

$$\frac{V_{i,j,k}}{\Delta t}\delta U^n_{i,j,k} + (A'_{+i+\frac{1}{2},j,k}\delta U_{i,j,k} - A'_{+i-\frac{1}{2},j,k}\delta U_{i-1,j,k}$$
$$+ A'_{-i+\frac{1}{2},j,k}\delta U_{i+1,j,k} - A'_{-i-\frac{1}{2},j,k}\delta U_{i,j,k})^n$$
$$+ (B'_{+i,j+\frac{1}{2},k}\delta U_{i,j,k} - B'_{+i,j-\frac{1}{2},k}\delta U_{i,j-1,k}$$
$$+ B'_{-i,j+\frac{1}{2},k}\delta U_{i,j+1,k} - B'_{-i,j-\frac{1}{2},k}\delta U_{i,j,k})^n$$
$$+ (C'_{+i,j,k+\frac{1}{2}}\delta U_{i,j,k} - C'_{+i,j,k-\frac{1}{2}}\delta U_{i,j,k-1}$$
$$+ C'_{-i,j,k+\frac{1}{2}}\delta U_{i,j,k+1} - C'_{-i,j,k-\frac{1}{2}}\delta U_{i,j,k})^n$$
$$- Z^n_{i,j,k}\delta U^n_{i,j,k} = \Delta U^n_{i,j,k} \tag{24}$$

where $\Delta U^n_{i,j,k}$ is the change in the solution due to the fluxes and the source term at time level n. This equation represents the discretized version of the extended Navier-Stokes equations. Picking an initial condition and specifying the boundary conditions, Eq. (24) can be solved for $\delta U^n_{i,j,k}$ and the solution advanced in time until a steady state is achieved.

Recently Yoon and Jameson[17] developed the lower-upper symmetric Gauss-Seidel (LU-SGS) or diagonal implicit scheme and Park and Yoon,[15] Eberhardt and Imlay,[13] and Imlay et al.[14] have extended the method to chemically reacting flows. They have reported very good convergence rates and small computational costs. The method is derived here, some im-

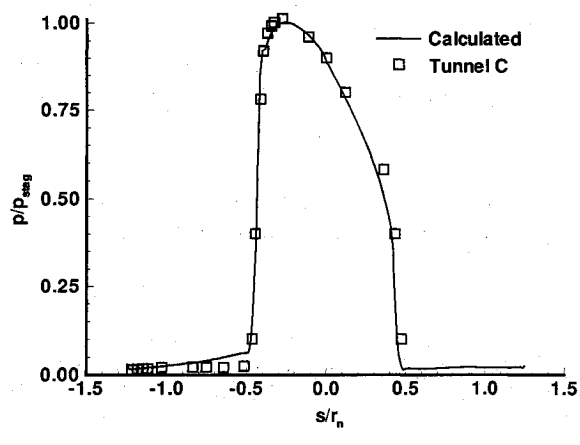

Fig. 4 Plane of symmetry pressure distribution for wind-tunnel validation case at 20-deg angle of attack, surface distance measured from centerline.

provements are suggested, and some of its attributes are discussed.

Consider the implicit difference equation, Eq. (24). Approximate the flux Jacobians that appear on the left-hand side of this equation in the following manner:

$$A'_{+i+\frac{1}{2},j,k} \simeq \tfrac{1}{2}[A'_{i,j,k} + \rho(A'_{i,j,k})I]$$
$$A'_{-i-\frac{1}{2},j,k} \simeq \tfrac{1}{2}[A'_{i,j,k} - \rho(A'_{i,j,k})I] \tag{25}$$

and similarly for the y and z direction fluxes. $\rho(A')$ is the spectral radius of A'; $\rho(A') = |u'| + a$, where u' is the velocity in the ξ direction and a is the local speed of sound. Similar expressions exist for B' and C'. Then, substituting

$$A'_{+i+\frac{1}{2},j,k} - A'_{-i-\frac{1}{2},j,k} \simeq \rho(A'_{i,j,k})I \tag{26}$$

for the Jacobians that multiply $\delta U_{i,j,k}$, the following is obtained:

$$\left[\frac{V_{i,j,k}}{\Delta t} + \rho(A'_{i,j,k}) + \rho(B'_{i,j,k}) + \rho(C'_{i,j,k}) - Z_{i,j,k}\right]^n \delta U^n_{i,j,k}$$
$$= \Delta U^n_{i,j,k} + (A'_{+i-\frac{1}{2},j,k}\delta U_{i-1,j,k} - A'_{-i+\frac{1}{2},j,k}\delta U_{i+1,j,k})^n$$
$$+ (B'_{+i,j-\frac{1}{2},k}\delta U_{i,j-1,k} - B'_{-i,j+\frac{1}{2},k}\delta U_{i,j+1,k})^n$$
$$+ (C'_{+i,j,k-\frac{1}{2}}\delta U_{i,j,k-1} - C'_{-i,j,k+\frac{1}{2}}\delta U_{i,j,k+1})^n \tag{27}$$

The spectral radii are scalars and, thus, aside from the Jacobian Z, all of the quantities multiplying $\delta U^n_{i,j,k}$ are scalars. Assuming that we can find a way of diagonalizing Z, then the solution procedure is as follows. Sweep through the flowfield from the lower left-hand corner to the upper right-hand corner to determine δU^{*n} according to

$$\delta U^{*n}_{i,j,k} = \mathfrak{D}^{-1}(\Delta U_{i,j,k} + A'_{+i-\frac{1}{2},j,k}\delta U^*_{i-1,j,k}$$
$$+ B'_{+i,j-\frac{1}{2},k}\delta U^*_{i,j-1,k} + C'_{+i,j,k-\frac{1}{2}}\delta U^*_{i,j,k-1})^n \tag{28}$$

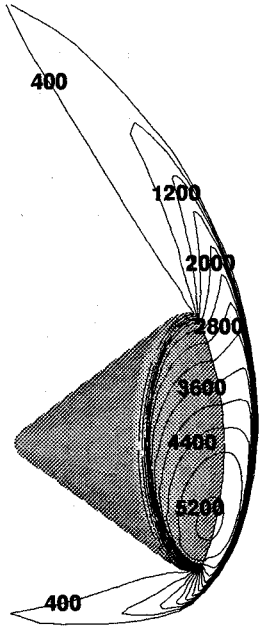

Fig. 5 Perfect gas pressure contours: contour levels vary between 0 and 5600 N/m² with 15 levels, inclusive.

where $\mathfrak{D}$ is defined as

$$\mathfrak{D} = \left[\frac{V_{i,j,k}}{\Delta t} + \rho(A'^n_{i,j,k}) + \rho(B'^n_{i,j,k}) + \rho(C'^n_{i,j,k}) - V_{i,j,k}\,\mathrm{diag}(Z^n_{i,j,k})\right] \tag{29}$$

Then perform the opposite sweep to find δU^n

$$\delta U^n_{i,j,k} = \delta U^{*n}_{i,j,k} - \mathfrak{D}^{-1}(A'_{-i+\frac{1}{2},j,k}\delta U_{i+1,j,k}$$
$$+ B'_{-i,j+\frac{1}{2},k}\delta U_{i,j+1,k} + C'_{-i,j,k+\frac{1}{2}}\delta U_{i,j,k+1})^n \tag{30}$$

Therefore, if we can find a way of diagonalizing Z, Eq. (21) can be solved with only one scalar inversion.

This procedure results in a rescaling of the local time step according to the size of

$$\tau = \mathfrak{D}^{-1} \tag{31}$$

Thus, for large Δt, the change in the solution will be limited by the size of the spectral radii of the flux Jacobians and some choice of the magnitude of Z.

One obvious way that would maintain diagonal dominance would be to replace $-Z$ with its spectral radius. There are two problems with doing this. First, the spectral radius of Z is difficult to determine analytically and, for typical flow conditions, it is very much larger than the spectral radii of A, B, and C. The latter problem results in very slow convergence rates because the effective local time step would be

$$\tau = \left[\frac{V_{i,j,k}}{\Delta t} + \rho(A'^n_{i,j,k}) + \rho(B'^n_{i,j,k}) + \rho(C'^n_{i,j,k}) + V_{i,j,k}\rho(Z^n_{i,j,k})\right]^{-1} \simeq \frac{1}{V_{i,j,k}\rho(Z^n_{i,j,k})} \ll \Delta t \tag{32}$$

Thus the maximum amount that the solution can change at each time step is extremely small. For example, typical flows will have $\rho(Z)/\rho(A') \approx 10^4$. Thus, 10^4 time steps must be taken to advance the solution to the same time level that is achieved in one time step if the flow is nonreacting. In other words, it costs about a factor of 10^4 to simulate reacting flows. Clearly, this is a poor way of representing diag(Z).

Eberhardt and Imlay[13] and Imlay et al.[14] recognized this problem and came up with an improvement that allowed them to obtain solutions to chemically reacting flows with only a small penalty. They approximated Z as a diagonal matrix, which for the five-species gas model discussed earlier has the form

$$Z \simeq \mathrm{diag}\left(\frac{1}{\tau_1}, \frac{1}{\tau_2}, \ldots, \frac{1}{\tau_5}, 0, 0, 0, \frac{1}{\tau_v}, 0\right) \tag{33}$$

where τ_s is the chemistry time scale for species s and τ_v is the time scale for vibrational relaxation. The choice of τ_s is suggested as

$$\frac{1}{\tau_s} = \beta_c\sqrt{\sum_{r=1}^{5}\left(\frac{\partial w_s}{\partial \rho_r}\right)^2}, \qquad s = 1, 2, \ldots, 5 \tag{34}$$

where β_c is a relaxation parameter to maintain stability of the solution. These authors have successfully simulated a wide range of hypersonic chemically reacting flows including both re-entry flows and flows with combustion.

Now consider the implications of the preceding method. First, note that each chemical species has a different chemical time scale and thus a different temporal relaxation rate. Therefore, the effective local time step for each chemical species will be different at each grid point. Now consider the

five-species air model. N_2 reacts much more slowly than O_2 and, therefore,

$$\tau_{N_2} \gg \tau_{O_2}$$

Because of this disparity in the chemical time scales, the density of N_2 will adjust much more quickly to convection-induced changes than does that of O_2. This results in a lack of elemental conservation from time step to time step. Also note that the sum of all species density equations results in the total density equation. The total density then has a local time step that is a weighted sum of the chemical time scales. Therefore, the total density can only evolve at the time step governed by the chemical time scales, which is much smaller than the time step at which the momentum and total energy are allowed to change. Therefore, the total density lags the evolution of the other flow variables which may lead to instability and a poor convergence rate. These two problems, elemental nonconservation and the lagging of the total density with respect to the other flow variables, result in less than optimal performance of the diagonal implicit scheme for chemically reacting flows.

With the equation set discussed in the previous section, we will see that the way in which Z is diagonalized is less critical. Using the terminology of Refs. 13 and 14, let us represent the diagonalized Z as

$$Z \simeq -\text{diag}\left(0, 0, \frac{1}{\tau_{NO}}, \frac{1}{\tau_N}, \frac{1}{\tau_O}, 0, 0, 0, \frac{1}{\tau_v}, 0\right) \tag{35}$$

Now, because we are solving for the elemental densities, elements are always conserved no matter how the three species NO, N, and O evolve during convergence to steady state. Also, because there is no chemistry source term for the elemental densities and because their sum is the total density, the total density can evolve at the same rate as the momentum and total energy. Therefore, the problem of the total density lagging the changes in the other variables is alleviated. Additionally, from experience, we find that the relaxation parameter β_c is no longer required in the expression for τ_s. Instead, use

$$\frac{1}{\tau_s} = \sqrt{\sum_{r=1}^{2}\left(\frac{\partial w_s}{\partial \tilde{\rho}_r}\right)^2 + \sum_{r=3}^{5}\left(\frac{\partial w_s}{\partial \rho_r}\right)^2} \tag{36}$$

and for the vibrational energy equation use

$$\frac{1}{\tau_v} = \left|\frac{\partial w_v}{\partial E_v}\right| \tag{37}$$

This approach may be generalized to more complicated thermochemical models. When ionization is included, a suitable choice of the additional elemental density due to the presence of electrons is the charge density.

For viscous calculations, the spectral radius of the viscous Jacobians is obtained from the work of Tysinger and Caughey.[27] Thus the following term

$$\frac{(\xi_x^2 + \xi_y^2 + \xi_z^2 + \eta_x^2 + \eta_y^2 + \eta_z^2 + \zeta_x^2 + \zeta_y^2 + \zeta_z^2)}{\phi V_{i,j,k}} \frac{\gamma\mu}{\rho Pr}$$

is added to the diagonal matrix $\mathfrak{D}$, and ϕ is defined as the circumferential angle between adjacent computational planes in the η direction.

Diagonal Implicit Comparison

Now consider the inviscid, chemically reacting flow over a 1-m radius cylinder with freestream conditions corresponding to 60-km altitude and 5-km/s flow velocity. A comparison of the diagonal implicit method of Eberhardt and Imlay[13] and Imlay et al.[14] with the proposed diagonal method will be made. The grid is 56×100 with points equally spaced around the 90-deg portion of the cylinder. The mesh is exponentially stretched from the wall with a mesh spacing at the stagnation point of 10^{-3} of the nose radius. The flow is initialized as freestream conditions, and the bow shock is allowed to form and move away from the body until it reaches its steady-state position.

The convergence history is presented in Fig. 1 for the two methods. For both methods, a Courant-Fredricks-Levy (CFL) number of 10 was used for the entire calculation. As discussed previously, no relaxation parameter on the chemical or vibrational source terms is required for the present method. However, for the method of Eberhardt, a relaxation parameter on the chemical source terms is required. This is denoted as β_c in Eq. (34). Various values of β_c were used in the course of the simulation. It was found that the maximum initial value for β_c was 0.1 for a stable solution. We see that this results in a convergence history that is coincident with the proposed method for about one order of magnitude reduction in the residual. Then the solution stops converging. If the solution after 500 iterations is used as an initial condition with $\beta_c = 0.5$, then the convergence continues and becomes similar to the proposed method. Further increasing β_c to 1.0 results in a worse convergence rate. Thus there is some optimal sequence of β_c that results in the best possible convergence rate. This rate, however, only approaches that of the proposed diagonal

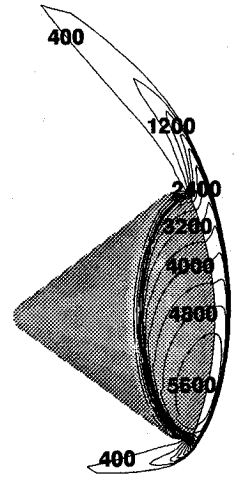

Fig. 6 Reacting gas pressure contours: contour levels vary between 0 and 5600 N/m² with 15 levels, inclusive.

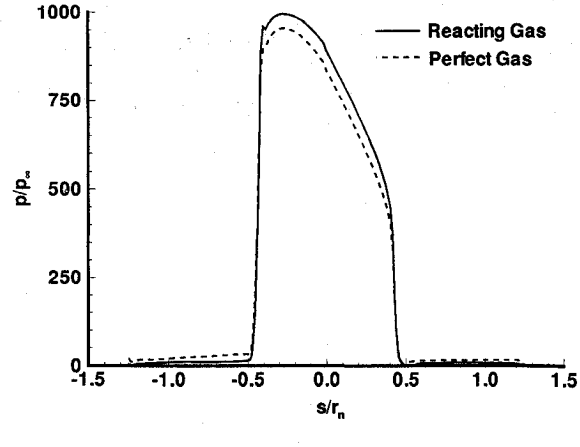

Fig. 7 Plane of symmetry pressure distributions, surface distance measured from centerline.

implicit algorithm. Therefore, the new method appears to perform better than the previous method.

However, Eberhardt and Imlay[13] and Imlay et al.[14] state that they limit the reactions in any one cell by artificially resetting the Damköler number. This technique was not employed in these calculations using the previous method and may be the cause for the less than optimal convergence behavior. Calculations have been made on other geometries since publication of the original paper using our present method and resetting the Damköler number. It was found that convergence was only initially accelerated when employed on sparse grids, and erratic convergence behavior was observed when the solution approached a steady state. No benefit was observed when there was adequate grid resolution in the boundary layer and in the shock region.

Apollo Command Module

The baseline geometry of the Apollo command module flown in the unmanned AS-202 mission is shown in Fig. 2. The forebody is a truncated sphere with rounded corners. On the actual flight geometry, a truncated spherical ablator is attached to the baseline shape with a 0.195-deg cant angle measured from the centerline.[4] This results in more ablative material on the windward side of the body where the heating rates are higher. Current calculations are made on a body assuming a symmetric ablator shape. However, no ablation occurred on this mission.

Wind-Tunnel Validation

To demonstrate code capability with wind-tunnel data, a case is presented comparing to pressure data obtained in Tunnel C at the Arnold Engineering and Development Center (AEDC) by Bertin.[28] The comparison test was run on a 0.045 scale model of the full-size vehicle at an angle of attack of 20 deg. Freestream conditions corresponded to a Mach number of 10.18 and Reynolds number based on maximum diameter of 1.1×10^6. To compute the flowfield, a perfect gas version of the present algorithm is used. The computational grid is shown in Fig. 3 and has 110 planes axially, 26 planes circumferentially, and 70 planes normal to the body. The mesh is exponentially stretched from the wall. The mesh spacing at the wall is 1/2000 the axial distance measured from the nose to the point of maximum diameter, i.e., the rear of the forebody. The inviscid fluxes are first-order accurate in the normal and circumferential directions. Second-order accuracy is obtained in the axial direction using a total variation diminishing minmod formulation found in Hirsch.[20] Laminar flow is assumed throughout and the wall temperature is set at 300 K.

Figure 4 shows the plane of symmetry pressure distribution. Plotted is the local-to-stagnation pressure ratio vs the surface distance, nondimensionalized by the nose radius, measured from the centerline. Excellent agreement is observed between the calculated data and the experimental data from Tunnel C. The maximum experimental pressure ratio at the stagnation point is seen to exceed unity slightly. The value used to normalize the data was the calculated value of the stagnation pressure behind a normal shock. The experimental stagnation pressure was slightly greater, thus leading to the discrepancy. A slight deviation between the present calculated pressure and the experimental data is observed on the conical afterbody on the windward side of the vehicle. No experimental data were given for the leeward side of the vehicle.

Flight and Wind-Tunnel Comparison

Now a comparison will be made between the flight and wind-tunnel conditions. Both the perfect gas and reacting gas results are presented. The reacting gas model consists of the five species discussed earlier. The calculations are made at the initial entry point of $t + 4480$ s into the trajectory at a Mach number of 27.2. Flight data show the trim angle of attack α to be 17.5 deg whereas the wind-tunnel data gives 21.0 deg. Here the flight data showed an 18% lower lift-to-drag ratio than that predicted by the wind-tunnel data.

Since wind tunnels could not reproduce the flight conditions at the initial entry high Mach number, low Reynolds number flight regime, preflight aerodynamic data were extrapolated to this region.[4] The maximum Mach number tested was 18.73 in the AEDC 50-in. Hot Shot II Tunnel.[29] An extensive amount of testing was done in the then Cornell Aeronautical Laboratories (CAL) 48-in. Hypersonic Shock Tunnel[30] at a Mach number of 15.75. The wind-tunnel geometry was 0.05 scale of the full-size configuration. In Table 1, a comparison of the freestream flight and tunnel conditions is made. Tabulated are the Mach number, Reynolds number based on maximum body diameter, and stagnation enthalpy. As previously mentioned, the difference in Mach number is evident. The freestream Reynolds numbers are comparable in each case, but there is an order of magnitude difference in stagnation enthalpy. The flight value is 14.3 times larger than that of the wind tunnel. This disparity in h_{0_∞} plays a major role in the type of flowfields that exist in each case. For lower enthalpy flows, there will not be sufficient energy in the flow to promote chemical reactions in the shock layer. However, for the higher enthalpy case, there will be sufficient energy to dissociate the molecules, and thus energy would be removed from the translational-rotational mode. This results in a lower peak shock layer translational-rotational temperature and higher density rise across the shock wave than would be obtained in the perfect gas case. Also of concern is the degree of nonequilibrium that may exist in the flow.

Table 1 Freestream flight and tunnel conditions

	AS-202 flight	CAL 48-in. tunnel
M_∞	27.2	15.75
Re_∞	194,111	233,268
h_{0_∞}, mj/kg	32.842	2.305

Therefore, to properly analyze the physics of each flow, the reacting gas code was run at the flight trim angle of attack, whereas the perfect gas code used the wind tunnel predicted trim angle of attack since it was a nonreacting gas simulation. Effects due to the sting mount have been neglected. The aerodynamic coefficients calculated are the lift coefficient C_L, the drag coefficient C_D, the lift-to-drag ratio $L/D = C_L/C_D$, and the pitching moment coefficient about the center of gravity $C_{M_{cg}}$. The center of gravity is located at an x distance of 1.070 m measured from the nose of the vehicle and a z distance of -0.132 m measured from the centerline.

Results and Discussion

The perfect gas grid is the same as shown in Fig. 3 but scaled to the full-size vehicle. Since the shock layers are thinner in the reacting gas cases, the freestream boundary for the reacting gas grid is closer to the body. The resulting grid is similar to the perfect gas grid but with only 65 planes normal to the body. Laminar flow is assumed throughout. The wall is noncatalytic and both T and T_v are set to a wall value of 1500 K. Expressions for the viscosity and thermal conductivities can be found in Candler.[10] The freestream is assumed to be composed of diatomic nitrogen and oxygen in the reacting gas case. The freestream velocity, density, and temperature are 8.08 km/s, 8.7535×10^{-5} kg/m^3, and 219.7 K, respectively. This corresponds to an altitude of approximately 70.1 km.

For the perfect gas case, the L_2 norm of the residual was converged three orders of magnitude in 7000 iterations, requiring 6.89 CPU h and 8.02 Mwords of memory on a Cray Y-MP. This corresponds to 17.7 μs/iteration/grid point and 40.0 words/grid point. For the reacting gas case, convergence was achieved in 13,000 iterations, requiring 23.5 CPU h and 13.5 Mwords of memory. This results in 35.0 μs/iteration/grid point and 72.6 words/grid point.

Figures 5 and 6 show the pressure contours in the plane of symmetry for the perfect gas and reacting gas cases, respectively. As previously mentioned, the shock layer is much thinner for the reacting gas case. This effect is much more pronounced on the leeward side and is a direct function of the

chemical reactions in the five-species air model. The difference in the shock shapes significantly affects the surface pressure distributions and thus the pitching moment coefficient and trim angle of attack. In both cases, the pressure in the afterbody region aft of the expansion is approaching the freestream value. The pressure distributions along the plane of symmetry are illustrated in Fig. 7. The reacting gas case predicts higher pressures over much of the forebody. Both cases approach the same value through the expansion, as illustrated in the previous contour plots. However, the perfect gas pressure is slightly higher over the afterbody. The differences in pressure, especially over the forebody, will significantly affect the lifting and drag forces on the vehicle.

In Fig. 8, both perfect gas and reacting gas temperatures are plotted vs distance along the stagnation line. The disparity in shock-layer thickness is again seen by the location of the temperature rise in each case. The maximum shock-layer temperatures for the perfect gas case are of the range of 33,000 K and are unrealistic for practical cases. Also shown are the translational-rotational temperature and the vibrational temperature for the reacting gas case. The maximum translational-rotational temperature across the shock wave is of the order of 15,000 K, whereas the peak T_v is about 11,000 K. Energy is transferred into dissociation and vibration and taken away from translation, thus reducing the translational-rotational temperature. The extent of thermal nonequilibrium can be seen as well. It is observed that the thermal nonequilibrium region is large and that equilibrium is not reached until near the wall region.

In addition, the chemical nonequilibrium can also be observed in the amount of dissociation that takes place in the flow. Figure 9 shows all the species mass fractions along the stagnation line. It is observed that only about 20% of the flow is diatomic nitrogen in the shock layer and boundary layer. This amount of dissociation can be expected due to the high flowfield temperatures. Diatomic oxygen is fully dissociated, thus the shock layer is primarily composed of N_2, N, and O. As expected, significant amounts of NO only exist in the shock region.

In Table 2, the aerodynamic coefficients predicted by the numerical solutions are compared with the flight and wind-tunnel values. The first two columns compare the reacting gas computation to the flight data at the flight trim angle of attack of 17.5 deg. From the comparison, we see a 7.3% overprediction in the lift coefficient and a 10.9% overprediction in the drag coefficient. This results in a 4.5% underprediction in L/D. More importantly, the pitching moment coefficient about the center of gravity $C_{M_{cg}}$ is of order 10^{-3} giving a near trim condition.

The perfect gas case calculation is compared to the extrapolated preflight wind-tunnel data in last two columns of Table 2. The numerical results compare well with the experimental data. The numerical C_L is underpredicted by 4.7%, but C_D is only overpredicted by 0.16%. Consequently, L/D is underpredicted by 5.0%. Finally, a near trim condition is also obtained at the wind-tunnel trim angle of attack of 21.0 deg.

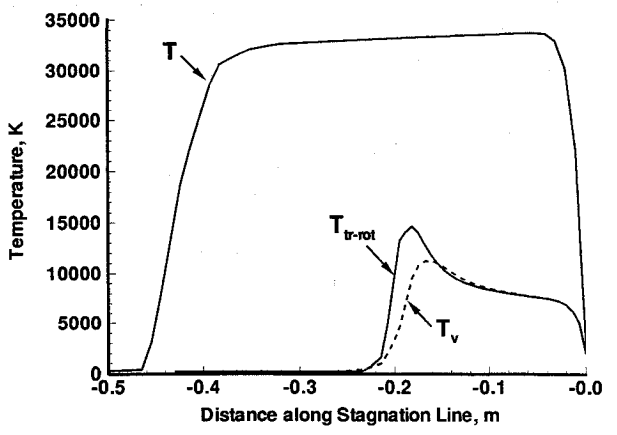

Fig. 8 Perfect gas temperature and reacting gas translational-rotational and vibrational temperatures along the stagnation line.

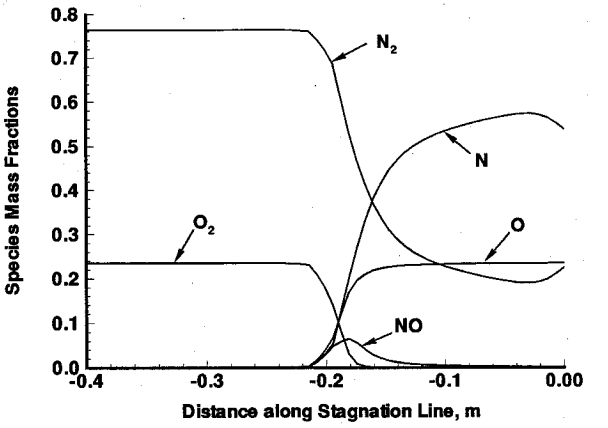

Fig. 9 Species mass fractions along the stagnation line.

Table 2 Aerodynamic coefficients comparison

	Five species air	AS-202 flight data	Perfect gas	Wind-tunnel data
α, deg	17.5	17.5	21.0	21.0
C_L	−0.354	−0.33	−0.387	−0.406
C_D	1.397	1.26	1.272	1.27
L/D	−0.253	−0.265	−0.304	−0.32
$C_{M_{cg}}$	−0.00135	0.0	−0.01220	0.0

Next, reasons for the discrepancies between the numerical and experimental results will be addressed. There are questions about the accuracy of the flight and tunnel data. Hillje[4] stated that there are a number of uncertainties in the flight data including inaccuracies in determining spacecraft position and c.g. location. This includes an error of ±30.48 m/s in velocity and ±0.04 deg in flight path angle. Furthermore, the wind-tunnel data are a culmination of data from different tunnels at various Mach numbers below 18.73. Various models were tested, some including asymmetries due to the heat shield, sting mounts, and protuberances. Comparisons at Mach numbers below 6 for models with and without protuberances showed trim angle differences of 3 deg or less.[29]

The numerical results could be improved by including better physical models. For the high Mach number, low density flows being considered, ionization effects need to be included, especially for the range of temperatures that were observed. Furthermore, though a symmetric configuration was modeled, previous calculations on the forebody at angles of attack plus or minus the ablator cant angle of 0.195 deg showed negligible change in the aerodynamic coefficients. Finally, grid resolution is always an important issue especially in drag calculations. Inviscid grid resolutions studies on the forebody showed slightly lower drag coefficients on denser grids.

In any case, we see that the numerical results predict the flight and wind-tunnel aerodynamic coefficients within the accuracy of the data. The results show that a lower trim angle of attack is produced by the reacting gas air model, as is indicated by the flight data. This reduction in trim angle corresponds to a lower L/D during re-entry. Therefore, real gas effects must be included to accurately predict entry flight aerodynamics.

Conclusions

Navier-Stokes calculations have been made to simulate the re-entry of the Apollo command module to determine the

effect of thermal and chemical nonequilibrium on the trim angle of attack and lift-to-drag ratio. Calculations were carried out assuming perfect gas and five-species reacting gas air models and compared with wind-tunnel and flight data, respectively. The reacting gas model assumed a two-temperature model to describe the internal energy modes. Reacting gas computations predicted aerodynamic coefficients within 10.9% at the flight trim angle of 17.5 deg at a Mach number of 27.2. Perfect gas analysis predicted the aerodynamic coefficients to within 5.0% of those obtained for the wind-tunnel trim angle of attack of 21.0 deg. The numerical results demonstrate that the trim angle and L/D for a reacting gas are lower than that predicted by a perfect gas and are consistent with the experimental data.

Also, the modified form of the diagonal implicit scheme presented was shown to be very robust for calculating the steady-state solutions for chemically reacting flows. Overall CPU times are comparable and memory usage is significantly less than other current implicit techniques.

In conclusion, numerical modeling of hypersonic flows has become increasingly important in the design of re-entry vehicles due to the high cost of flight experiments and lack of adequate ground testing facilities. Using CFD, the effects of chemical reactions and vibrational excitation on the aerodynamics of aerobraking vehicles have been shown. Finally, by comparison to the available experimental data, the limitations of physical models can be determined, and how much confidence that can be placed in numerical solutions can be assessed.

Acknowledgments

This work is supported in part by the following grants: NASA Langley Research Center Cooperative Agreement NCC1-140 with the Aerothermodynamics Branch of the Space Systems Division, and NASA Grant NAGW-1331 to the Mars Mission Research Center at North Carolina State University. Computer time was provided by the North Carolina Supercomputing Center. The authors would like to thank Peter A. Gnoffo of the Aerothermodynamics Branch at NASA Langley Research Center for his many helpful discussions. In addition, the primary author would like to extend thanks to Kevin Moore of the North Carolina Supercomputing Center for providing much needed technical support on the Cray Y-MP.

References

[1]Braun, R. D., "The Effect of Interplanetary Options on a Manned Mars Aerobrake Configuration," M.S. Thesis, George Washington Univ., Washington, DC, Aug. 1989.

[2]Tauber, M., Chargin, M., Henline, W., Chiu, A., Yang, L., Hamm, K. R., Jr., and Miura, H., "Aerobrake Design Studies for Manned Mars Missions," AIAA Paper 91-1334, June 1991.

[3]Walberg, G. D., "Aerocapture for Manned Mars Missions—Status and Challenges," AIAA Paper 91-2870, Aug. 1991.

[4]Hillje, E. R., "Entry Flight Aerodynamics From Apollo Mission AS-202," NASA TN D-4185, Oct. 1967.

[5]Hillje, E. R., "Entry Aerodynamics at Lunar Return Conditions Obtained from the Flight of Apollo 4 (AS-501)," NASA TN D-5399, Oct. 1969.

[6]Lee, D. B., and Goodrich, W. D., "The Aerothermodynamic Environment of the Apollo Command Module during Suborbital Entry," NASA TN D-6792, April 1972.

[7]Park, C., and Yoon, S., "Calculation of Real-Gas Effects on Blunt-Body Trim Angles," AIAA Paper 89-0685, Jan. 1989.

[8]Gnoffo, P. A., "An Upwind-Biased, Point-Implicit Relaxation Algorithm for Viscous, Compressible Perfect-Gas Flows," NASA TP-2953, Feb. 1990.

[9]Gnoffo, P. A., Gupta, R. N., and Shinn, J. L., "Conservation Equations and Physical Models for Hypersonic Air Flows in Thermal and Chemical Nonequilibrium," NASA TP-2867, Feb. 1989.

[10]Candler, G. V., "The Computation of Weakly Ionized Hypersonic Flow in Thermo-Chemical Nonequilibrium," Ph.D. Thesis, Stanford Univ., Stanford, CA, June 1988.

[11]Candler, G. V., "Computation of Thermo-Chemical Nonequilibrium Martian Atmospheric Entry Flows," AIAA Paper 90-1695, June 1990.

[12]MacCormack, R. W., "Solution of the Navier-Stokes Equations in Three Dimensions," AIAA Paper 90-1520, June 1990.

[13]Eberhardt, S., and Imlay, S. T., "A Diagonal Implicit Scheme for Computing Flows with Finite-Rate Chemistry," AIAA Paper 90-1577, June 1990.

[14]Imlay, S. T., Roberts, D. W., Soetrisno, M., and Eberhardt, S., "Nonequilibrium Thermo-Chemical Calculations using a Diagonal Implicit Scheme," AIAA Paper 91-0468, Jan. 1991.

[15]Park, C., and Yoon, S., "A Fully-Coupled Implicit Method for Thermo-Chemical Nonequilibrium Air at Sub-Orbital Flight Speeds," AIAA Paper 89-1974, June 1990.

[16]Yoon, S., and Kwak, D., "An Implicit Three-Dimensional Navier-Stokes Solver for Compressible Flows," AIAA Paper 91-1555, June 1991.

[17]Yoon, S., and Jameson, A., "An LU-SSOR Scheme for the Euler and Navier-Stokes Equations," AIAA Paper 87-0600, Jan. 1987.

[18]Candler, G. V., and Olynick, D. R., "Hypersonic Flow Simulations Using a Diagonal Implicit Method," *Proceedings of the 10th International Conference on Computing Methods in Applied Sciences and Engineering* (Paris), edited by R. Glowlinski, Nova Science, New York, 1991, pp. 29–48.

[19]Anderson, D. A., Tannehill, J. C., and Pletcher, R. H., *Computational Fluid Mechanics and Heat Transfer,* McGraw-Hill, New York, 1984, pp. 185–186.

[20]Hirsch, C., *Numerical Computation of Internal and External Flows, Vol. 2: Computational Methods for Inviscid and Viscous Flows,* Wiley, New York, 1984, pp. 542, 543, 597–599.

[21]Park, C., "On Convergence of Computation of Chemically Reacting Flows," AIAA Paper 85-0247, Jan. 1985.

[22]Vincenti, W. G., and Kruger, C. H., Jr., *Introduction to Physical Gas Dynamics,* Krieger Publishing, Malabar, FL, 1965, p. 204.

[23]Millikan, R. C., and White, D. R., "Systematics of Vibrational Relaxation," *Journal of Chemical Physics,* Vol. 39, No. 12, 1963, pp. 3209–3213.

[24]Steger, J., and Warming, R. F., "Flux-Vector Splitting of the Inviscid Gasdynamics Equations with Application to Finite Difference Methods," NASA TM-78605, July 1979.

[25]MacCormack, R. W., and Candler, G. V., "The Solution of the Navier-Stokes Equations Using Gauss-Siedel Line Relaxation," *Computers and Fluids,* Vol. 17, No. 1, 1989, pp. 135–150.

[26]Van der Vegt, J. J. W., "Assessment of Flux Vector Splitting for Viscous Compressible Flows," AIAA Paper 91-0243, Jan. 1991.

[27]Tysinger, T. L., and Caughey, D. A., "Implicit Multigrid Algorithm for the Navier-Stokes Equations," AIAA Paper 91-0243, Jan. 1991.

[28]Bertin, J. J., "The Effect of Protuberances, Cavities, and Angle of Attack on the Wind-Tunnel Pressure and Heat-Transfer Distribution for the Apollo Command Module," NASA TM X-1243, Oct. 1966.

[29]Moseley, W. C., Jr., Moore, R. H., Jr., and Hughes, J. E., "Stability Characteristics of the Apollo Command Module," NASA TN D-3890, March 1967.

[30]Wilkinson, D. B., "Hypersonic Shock Tunnel Tests of the .05 Scale Apollo Force Model FS-8," Cornell Aeronautical Lab. Rept. AA-1712-W-1, Buffalo, NY, Oct. 1962.

E. Vincent Zoby
Associate Editor